Molecular Basis for the Cu^{2+} Binding-Induced Destabilization of β2-Microglobulin Revealed by Molecular Dynamics Simulation

Nan-Jie Deng, Lisa Yan, Deepak Singh, and Piotr Cieplak
Accelrys Inc., San Diego, California 92121

ABSTRACT According to experimental data, binding of the Cu^{2+} ions destabilizes the native state of β2-microglobulin (β2m). The partial unfolding of the protein was generally considered an early step toward fibril formation in dialysis-related amyloidosis. Recent NMR studies have suggested that the destabilization of the protein might be achieved through increased flexibility upon Cu^{2+} binding. However, the molecular mechanism of destabilization due to Cu^{2+}, its role in amyloid formation, and the relative contributions of different potential copper-binding sites remain unclear. To elucidate the effect of ion ligation at atomic detail, a series of molecular dynamics simulations were carried out on apo- and Cu^{2+}-β2m systems in explicit aqueous solutions, with varying numbers of bound ions. Simulations at elevated temperatures (360 K) provide detailed pictures for the process of Cu^{2+}-binding-induced destabilization of the native structure at the nanosecond timescale, which are in agreement with experiments. Conformational transitions toward partially unfolded states were observed in protein solutions containing bound copper ions at His-31 and His-51, which is marked by an increase in the protein vibrational entropy, with $T\Delta S$(vibr) ranging from 30 to 69 kcal/mol. The binding of Cu^{2+} perturbs the secondary structure and the hydrogen bonding pattern disrupts the native hydrophobic contacts in the neighboring segments, which include the β-strand D2 and part of the β-strand E, B, and C and results in greater exposure of the D-E loop and the B-C loop to the water environment. Analysis of the MD trajectories suggests that the changes in the hydrophobic environment near the copper-binding sites lower the barrier of conformational transition and stabilize the more disordered conformation. The results also indicate that the binding of Cu^{2+} at His-13 has little effect on the conformational stability, whereas the copper-binding site His-31, and to a lesser extent His-51, are primarily responsible for the observed changes in the protein conformation and dynamics.

INTRODUCTION

Metal ions are known to be essential to the function of enzymes and other classes of proteins. Ions bound to specific sites in proteins can profoundly alter the stability and structure of the protein through direct interaction with neighboring residues. In many proteins, metal ions interact simultaneously with several interior groups, stabilizing the local structure of the binding sites (1,2).

On the other hand, metal ions may also bind to partially exposed groups at the protein surface for which the ions have sufficient intrinsic affinity. Here, the ionic effect on the protein structure can be subtle, as ions have a strong affinity for water. The hydrophobic signature near the binding sites can be modified by the bound ion, which may induce structural changes that promote fluctuations in certain regions of proteins (3,4).

In this work we present results obtained from molecular dynamics (MD) simulations applied to study the structure, dynamics, and stability of β2-microglobulin (β2m) as a function of copper ion, Cu^{2+}, binding to residues that are either partially or completely exposed to water. Human β2m is known to form amyloidal fibrils under suitable conditions and is responsible for kidney dialysis-related amyloidosis (DRA), a serious disorder commonly found in patients receiving long-term hemodialysis (5).

The β2m protein is the light chain of the class I major histocompatibility (MHC-I) complex. It has 99 residues and adopts the immunoglobulin fold with seven β-strands forming a β-sandwich in its native state. The structure is stabilized by interactions between two β-sheets and a disulphide bond between Cys-25 and Cys-80 (6). One β-sheet consists of strands A, B, D, and E; the other is formed by strands C, F, and G. After its release as a globular protein from the cells displaying MHC-I, the β2m is carried to the kidney where it is degraded. When renal failure occurs, serum levels of β2m can increase significantly, and the normally soluble protein undergoes intermolecular association to form amyloid fibrils (7). However, higher concentration alone is not sufficient for amyloid formation, and in vitro studies have shown that at neutral pH and ionic conditions of the serum, the propensity of fibril formation is negligible (7,8). Hence extensive studies have been focused on finding external factors that promote amyloidosis. These include an acidic pH (9) and the shortening of the N-terminal by six residues (10). The presence of the Cu^{2+} ion at neutral pH was found to significantly enhance the fiber formation in vitro (11), a finding supported by clinical evidence that incidence of DRA is lower by 50% among patients treated by Cu^{2+}-free dialysis membrane. Using mass spectroscopy and fluorescence, Morgan et al. (11) demonstrated that β2m binds specifically to Cu^{2+}, whereas the binding of other divalent cations such as Ca^{2+} and Zn^{2+} is

Submitted June 14, 2005, and accepted for publication January 25, 2006.

Address reprint requests to Nan-Jie Deng, E-mail: ndeng@accelrys.com.

Piotr Cieplak's present address is The Burnham Institute for Medical Research, La Jolla, CA 92037.

0006-3495/06/06/3865/15 $2.00

doi: 10.1529/biophysj.105.064444

nonspecific. The Cu^{2+}-β2m dissociation constant is estimated to be 2.7 μm. They have also shown that the native protein is strongly destabilized against thermal and urea denaturation in the presence of Cu^{2+}.

After the first study on the Cu^{2+} effect, several reports have been published on the application of NMR and other experimental methods to explore the conformation and dynamics of β2m protein upon ion binding. Verdone et al. have shown that the protein binds Cu^{2+} at His-13 and His-31 at pH 6.6, as indicated by the change in the ^{1}H two-dimensional (2D) TOCSY (total correlation spectroscopy) spectrum (12). Eakin et al. studied the effect of several divalent cations and found that β2m was specifically destabilized by Cu^{2+} (13). Their study suggested that His-31 is the only histidine residue involved in the binding of copper in the native state, whereas the nonnative states of β2m bind Cu^{2+} at His-13, His-51, and His-84. They concluded that increased affinity for copper ion stabilizes nonnative states, which leads to the destabilization of native protein.

A recent heteronuclear NMR study (14) showed that at pH 7.0, three out of four histidines, His-13, His-31, and His-51 are involved in ion binding, whereas at pH 6.5, only His-13 and His-31 bind Cu^{2+}. This study reported increased backbone dynamics for the residues located between Val-49 and Ser-55, which is attributed to the binding of Cu^{2+} at His-51. Using hydrogen-deuterium exchange of amide protons, increased flexibility of the core residues was observed. The authors proposed that Cu^{2+} binding increases the pico- to nanosecond fluctuations of the β-strand D including His-51, which is propagated to the core residues and thus accelerates the overall destabilization of the protein.

Binding of divalent metals such as Cu^{2+} and Zn^{2+} has also been linked to amyloid formation in other systems, which include aggregation of Aβ in Alzheimer's disease (15,16), the prion protein (17), and the aggregation of the pathogenic immunoglobulin light chain (18). These findings suggest that the effects of divalent ion binding in different systems may share a common theme.

Despite numerous studies on the effect of Cu^{2+}, key questions remain to be answered to understand the full microscopic picture of the ionic effect. Although increased chain mobility was reported for the residues near His-51 upon Cu^{2+} binding (14), the physical picture for this is not well understood and to some extent counterintuitive, since the binding of metal ions usually tends to rigidify the local structure and provides a stabilizing effect to the native conformation. It is also puzzling why a similar increase in chain flexibility has not been observed for residues near the other ion-binding sites His-13 and His-31. As discussed above, several studies reported different copper-binding sites in the native state of β2m. Finally, different mechanisms were proposed for the driving force of the ionic destabilization. The study by Eakin et al. showed that an increased affinity for the Cu^{2+} ion at His-13, His-31, and His-84 in the unfolded states compared to the native state drives the overall destabilization (13), whereas Villanueva et al. found that the destabilization is mainly induced by the Cu^{2+} binding to the native state (14) and the His-51-binding site plays a critical role in the changes in structure and dynamics.

To date, there has been little information about the detailed picture of copper-ion-induced structural transitions. Although some knowledge on the dynamics of the protein can be inferred from NMR (19), information at atomic level has eluded observation since, in the Cu^{2+}-β2m system, the NMR spectra analysis has been complicated by the perturbation from paramagnetic metal ions (14). In this regard, MD simulations are well suited to probe the structural changes and dynamic processes of proteins at atomistic detail in the nanosecond timescale. This method is also widely used to gain information on the solvent environment, which can be perturbed by various factors. Another advantage of this method is that the researcher testing the validity of a specific hypothesis can vary a specific condition of interaction within the molecular system. In our case, assuming that the contributions from each ion-binding site are additive, we can study the relative contribution of different ion-binding sites to the overall destabilization by performing simulations with different ion-binding configurations and content.

In this study, we focus on the molecular picture of the Cu^{2+} ion-binding effect on the structure and dynamics of the β2m protein. We have performed six MD simulations of the apo-β2m and the Cu^{2+}-β2m in aqueous solution at 360 K temperature for a total of 24 ns. Elevated temperature allows richer dynamic processes to be studied by MD simulations in the nanosecond timescale. The results presented here show a correlation between the contents of bound Cu^{2+} ions and protein flexibility. The molecular driving forces for the Cu^{2+}-binding-induced destabilization are discussed in relation to these findings.

METHODS

Modeling the ion-protein complex

The first frame in the NMR solution structure family of human β2m (Protein Data Bank (PDB) identification no. 1jnj) was used as the starting conformation for simulation (12). The four histidines (His-13, His-31, His-51, and His-84) are in the neutral Nε2H tautomeric state in the NMR structure. It has been shown experimentally that binding of the Cu^{2+} ion does not occur at His-84 under native conditions (12,14).

Since the structure of the Cu^{2+}-β2m complex was not available, the initial configuration of the Cu^{2+}-binding sites at the three histidines (His-13, His-31, and His-51) were prepared as follows: a Cu^{2+} ion was first placed at the position which would be occupied by the δ1 hydrogen atom in the imidazole group of a protonated histidine. The Cu^{2+} ion was then pulled away from the bound nitrogen atom along the direction of the δ1H-N bond until the Cu^{2+}-N distance reached 2.1 Å, which is the averaging coordination bond length for Cu^{2+} nitrogen surveyed from several copper-containing protein structures in the PDB.

To model the coordination bond between the Cu^{2+} and the bound nitrogen atom in our simulations, a harmonic restraint with a flat bottom potential was applied between Cu^{2+} and the bound nitrogen atom. The

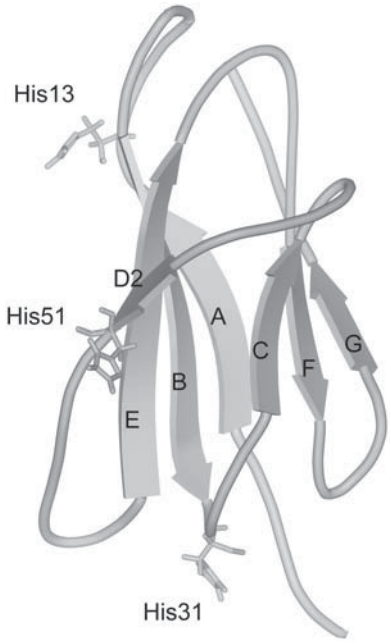

FIGURE 1 Diagram of the NMR structure of β2m, showing the labeling of the β-strands and the three Cu^{2+}-binding histidines. Note the less stable D1 strand is absent from the structure.

constraining potential was set to zero in the region between 2 and 3 Å, i.e., within this region, the Cu^{2+} interacts with its environment only through van der Waals and electrostatic forces. The nuclear Overhauser (NOE) distance restraint in the CHARMM program (20) was used for this purpose. The form of the constraining potential $E(r)$ is

$$\text{for } r < r_{\min},\ E(r) = \frac{1}{2}k_{\min}(r - r_{\min})^2;$$

$$\text{for } r_{\min} \le r \le r_{\max},\quad E(r) = 0;$$

$$\text{for } r_{\max} < r \le r_{\lim},\ E(r) = \frac{1}{2}k_{\max}(r - r_{\max})^2;$$

$$\text{and for } r_{\lim} < r,\ E(r) = f_{\max}\left(r - \frac{r_{\lim} + r_{\max}}{2}\right).$$

Here $r_{\min} = 2$ Å, $r_{\max} = 3$ Å, $k_{\min} = k_{\max} = 50$ kcal/mol × Å^2, $f_{\max} = 100$ kcal/mol × Å, and $r_{\lim}$ is the value of r where the force equals $f_{\max}$. All the simulated systems including solvents were otherwise unconstrained.

TABLE 1 Naming convention and residue composition of the β-strands in β2m

β-Strand name	Residue range
A	6–11
B	21–30
C	35–40
D1*	45–46
D2	50–51
E	62–70
F	79–84
G	91–94

*The D1 strand has ~50% occupancy in the NMR structure family.

TABLE 2 Summary of the simulations of β2m in explicit water

Name	Sites of bound Cu^{2+}	Simulation length (ns)	Counterions
0Cu	None	4	None
2Cu	His-13,His-31	4	2 Cl^-
3Cu	His-13,His-31,His-51	4	4 Cl^-
H-13	His-13	4	2 Cl^-, 2 Na^+
H-31	His-31	4	2 Cl^-, 2 Na^+
H-51	His-51	4	2 Cl^-, 2 Na^+

Molecular dynamics simulation

The CHARMm program (Accelrys, San Diego, CA) (20) version 29b1 was used to perform MD simulations in this study. The protein was modeled with the all-atom charmm22 parameter set (21). The van der Waals parameter of Cu^{2+} in the CHARMm force field (22) and a partial charge of +2e were used to model the nonbonded interaction involving copper ions. All the simulations were carried out under periodic boundary conditions, with β2m or Cu^{2+}-β2m complex solvated in a 70.14-Å truncated octahedral box of water. The distance between any protein atom and an edge of the water box was at least 9 Å. The TIP3P water model (23) was used to represent the solvent in the simulations. Waters within 2.8 Å of solute atoms were removed during the solvation process, and the final water box contained 8221 water molecules. The protein β2m (and thus the 0Cu system in Table 2) has

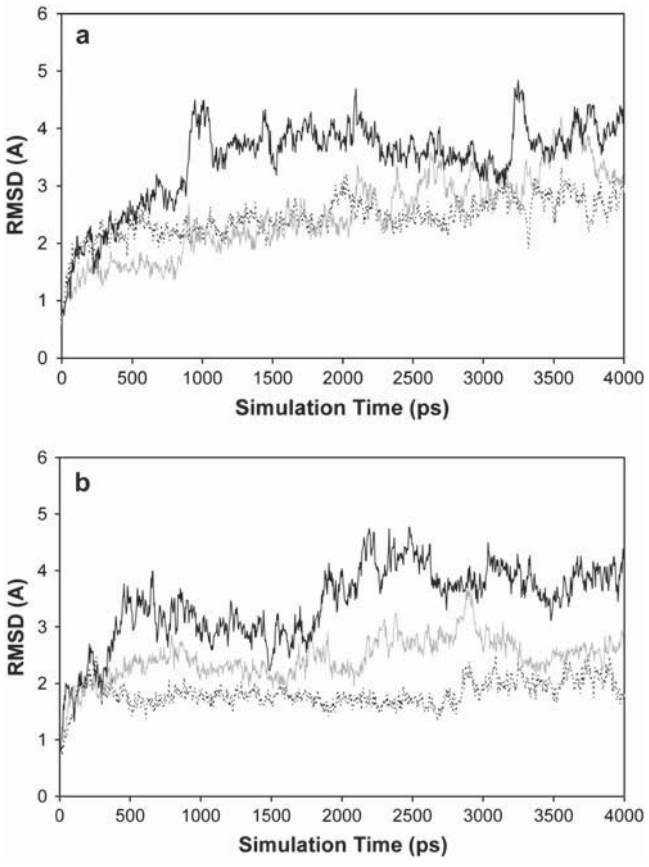

FIGURE 2 RMS deviations of Cα atoms from the starting structure as a function of the simulation time. (*a*) 0Cu (*black*, *dashed*), 2Cu (*gray*, *solid*), and 3Cu (*black*, *solid*). (*b*) H-13 (*black*, *dashed*), H-51 (*gray*, *solid*), and H-31 (*black solid*).

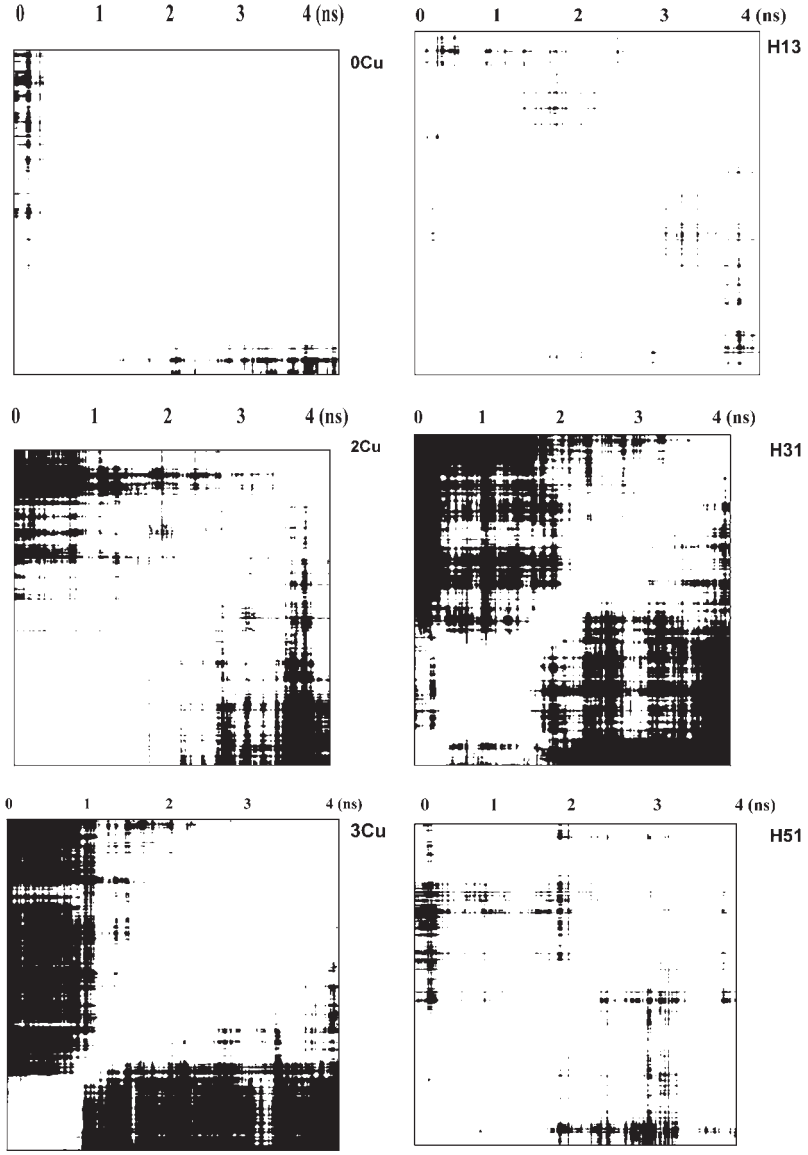

FIGURE 3 Pairwise Cα RMSDs between structures along trajectories. The two axes represent simulation time. Black area, RMSD $>$ 2.8 Å; white area, RMSD $\leq$ 2.8 Å.

a net charge of -2e. Counterions were added at random initial positions to keep the Cu^{2+}-β2m systems neutral (Table 2).

The electrostatic interactions were computed using the particle mesh Ewald (PME) method (24). A shift function was used to taper the van der Waals potential at 11.5 Å. The nonbond pair list was updated only when necessary by using a heuristic testing method in the CHARMm program. MD simulations were performed in the NpT ensemble, under atmospheric pressure, using constant pressure/temperature (CPT) dynamics. In this method, the conditions of CPT were achieved through the extended system approach developed by Nose and Hoover (25). Compared with other temperature-scaling schemes, the Hoover method of constant temperature control has the advantage of generating a rigorous canonical ensemble and continuous dynamics. The integration time step for MD was 1 fs.

The following thermal equilibration protocol was used to prepare the molecular system for the MD production run: With the solute fixed, the solvent was minimized for 1000 steepest descent steps and 1000 adopted basis Newton-Raphson (ABNR) steps. The constraints on the solute were then removed, and the whole system was minimized for 1000 steepest descent steps and 1000 ABNR steps. After the minimization, the system was heated to the desired temperature, 360 K, from 50 K within 20 ps. The system was then equilibrated at the target temperature for 40 ps before the production run was started. The trajectory was saved every 0.5 ps.

Secondary structure analysis was carried out using a utility program in DS Modeling 1.1 (Accelrys), which employs the Kabsch and Sander method (26). All the structure views in this study were generated with DS Modeling 1.1. Trajectory analysis was performed using the analysis module in CHARMm.

RESULTS

The native conformation of the β2m from NMR is shown in Fig. 1, which was used as the starting structure in the simulations. The naming convention and the residue composition of the β-strands are given in Table 1.

Thermal denaturation experiments of β2m indicate that the T_m is around 330 K (14). In this study, MD simulations were performed at 360 K on systems having different copper-ion-binding configurations. Table 2 summarizes these simulations.

TABLE 3 TS(vibr) calculated at different trajectory lengths

	1 ns*	1.5 ns	2 ns	2.5 ns	3 ns	3.5 ns	4 ns
0Cu	1469	1702	1831	1912	1970	2012	2051
2Cu	1456	1695	1829	1926	1993	2043	2083
3Cu	1474	1745	1883	1967	2029	2078	2118
H-13	1475	1708	1832	1907	1967	2015	2055
H-31	1490	1738	1876	1974	2036	2081	2120
H-51	1454	1690	1816	1904	1978	2031	2068

*Units, kcal/mol.

To verify that the simulation protocol and parameters were reasonable, a control MD run on apo-β2m at 300 K was performed for 3 ns in explicit water. The protein did not significantly deviate from the native structure throughout the course of simulation, and the averaged root mean square deviation (RMSD) for Cα atoms for the last 2.5 ns was 2.1 Å.

Overall conformational properties

The time dependence of the RMSD for Cα atoms from initial structures revealed substantial differences in the dynamics of the simulated systems (Fig. 2, *a* and *b*). For the 0Cu system, the RMSD remained within 2–3 Å from the starting structure, indicating that the protein did not move away significantly from the native conformation. The RMSD for H-13 was below 2.5 Å for most of the trajectory. There was no clear sign of major conformational transition for these two systems in the 4-ns simulation.

Larger fluctuations were observed in the 2Cu system, which showed two major rises in RMSD value within the 4-ns simulation. The first increase was a jump from 1.5 Å to 2.2 Å between 0.8 ns and 0.9 ns, which corresponds to a conformational change associated with the disruption of a short-lived β-strand comprising residues 55–56. The second rise in RMS value was more gradual, with the value increasing from 2.2 Å to 4.1 Å between 2.1 ns and 3.8 ns. As discussed later, this rise in RMSD reflects an increased disorder in the segments linking strand E and D2 (Figs. 7 *a* and 8 *a*).

The 3Cu and H-31 systems showed the largest fluctuations. In the 3Cu system, the RMSD increased from 3 Å to 4.5 Å between 0.88 ns and 0.96 ns. In H-31, the first major increase in RMSD occurred at 0.5 ns, which was followed by a second rise at between 1.8 ns and 1.95 ns. As discussed below, these increases in atomic motion correspond to transitions to less compact conformations which are more disordered in several parts of the protein, marking an early event in the unfolding of the protein. The RMS deviations then stay within 3.5–4.6 Å for most of the time during the rest of the simulations. The atomic fluctuations in the H-51 system are larger than those in the H-13 system but are smaller than those in the 2Cu, H-31, and 3Cu systems.

To gain more insight into the conformational changes, we calculated the Cα RMS deviations between the structures sampled along the trajectory and projected the data onto a 2D map (Fig. 3). A cutoff value of 2.8 Å was used to classify major conformational clusters visited in the simulation. In the 3Cu map, two adjacent white squares appeared along the diagonal, which is a clear sign for the existence of two clusters sampled consecutively along the trajectory. The first cluster persisted until 0.85 ns, and the second cluster was populated from 0.85 ns to 4 ns, which confirms the transition seen in Fig. 2. Similar behavior can be seen from the map for the H-31 simulation, where the two diagonally adjacent white blocks appear at ~1.8 ns, which coincides with the second major rise in RMSD as seen in Fig. 2.

In the 2Cu map, small black islands began to emerge from 2.5 ns along the time axis and grew to a larger connected area

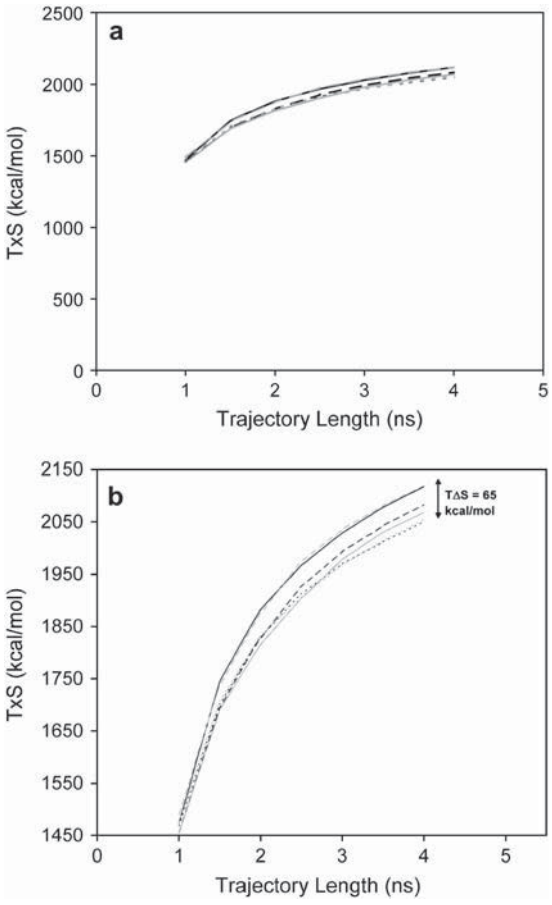

FIGURE 4 Vibrational entropy for different simulated systems: (*a*) Convergence with the trajectory length; (*b*) Detailed view where the differences among systems are more visible. The color codes are 0Cu (*black*, *dashed*), 2Cu (*black*, *broken*), 3Cu (*black*, *solid*), H-13 (*gray*, *dashed*), H-51 (*gray*, *broken*), H-31 (*gray*, *solid*).

TABLE 4 Net change in vibrational entropy TΔS(vibr) relative to 0Cu simulation

	0Cu*	2Cu	3Cu	H-13	H-31	H-51
TΔS(vibr)	0	32	67	4	69	17

*Units, kcal/mol.

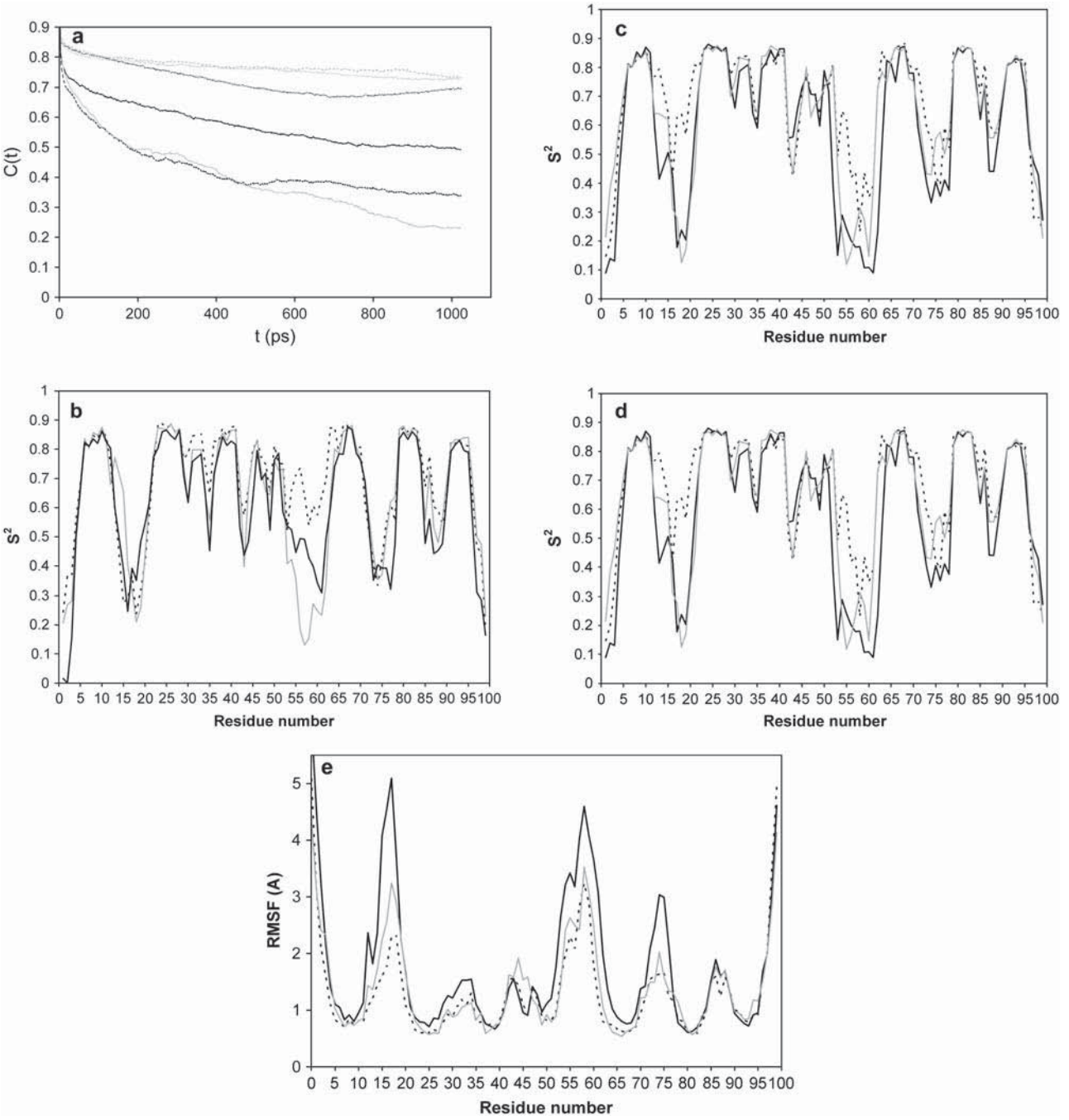

FIGURE 5 (*a*) Autocorrelation function C(*t*) for residue 62, the color codes are the same as those in Fig. 4 *b*. (*b*) NMR order parameter S^2 for 0Cu (*black*, *dashed*), 2Cu (*gray*, *solid*), and 3Cu (*black*, *solid*). (*c*) Same as in (*b*) for H-13 (*black*, *dashed*), H-51 (*gray*, *solid*), and H-31 (*black solid*). (*d*) Cα RMSF for 0Cu (*black*, *dashed*), 2Cu (*gray*, *solid*), and 3Cu (*black*, *solid*). (*e*) Same as in (*d*) for H-13 (*black*, *dashed*), H-51 (*gray*, *solid*), and H-31 (*black solid*).

from 3.3 ns. This indicated that from 2.5 ns onward the system started to sample conformational states that are significantly dissimilar from those sampled early in the simulation, consistent with the results in Fig. 2. Only isolated black spots were seen from the 0Cu and H-13 maps, indicating that the fluctuation in conformation is limited throughout the 4-ns trajectory. The H-51 map showed somewhat greater variations in the sampled conformations than those in the 0Cu and H-13 simulations.

Estimation of protein vibrational entropy

Considerations of the changes in entropy enable the conformational properties to be compared on a quantitative

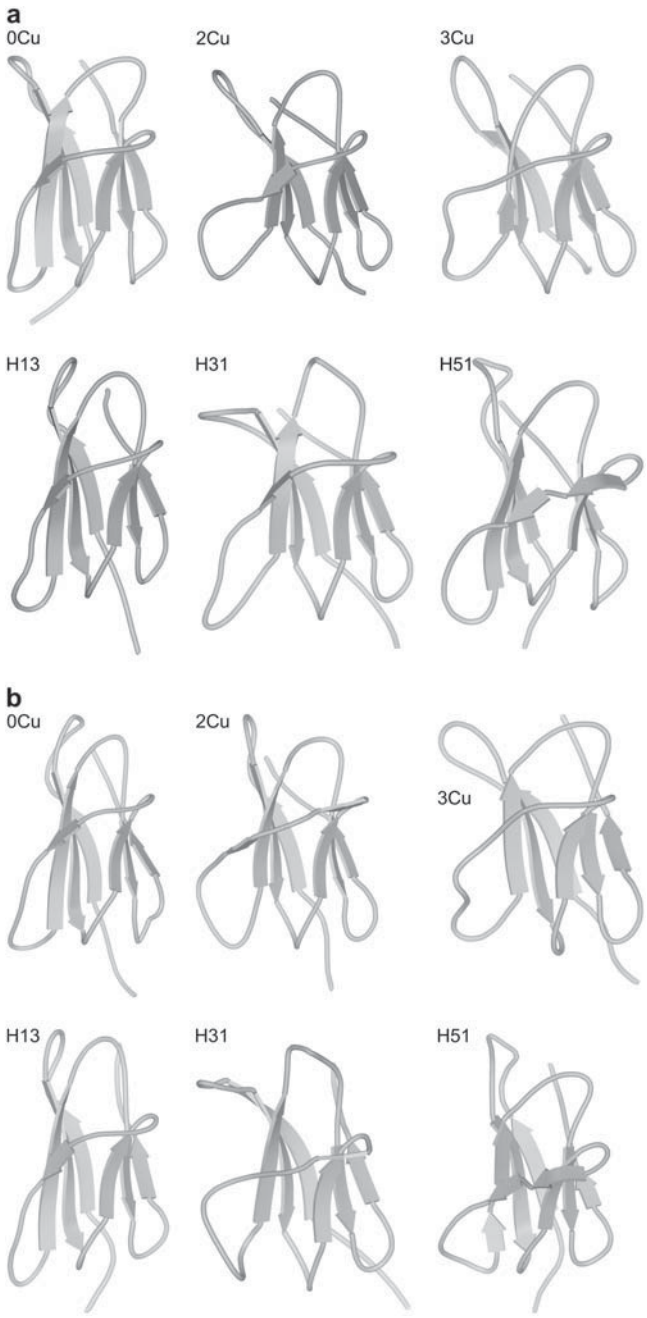

FIGURE 6 Main chain conformations of the simulated systems sampled at (*a*) 3.5 ns and (*b*) 4 ns.

basis. The total entropy of a protein molecule in solution includes contributions from both protein and solvent and can be written as

$$\mathrm{S(total)} = \mathrm{S(trans)} + \mathrm{S(rot)} + \mathrm{S(conf)} + \mathrm{S(vibr)} + \mathrm{S(solv)} \quad (1)$$

where S(trans), S(rot), and S(vibr) are the protein translational, rotational, and vibrational entropy, respectively. The protein conformational entropy S(conf) takes into account the fact that a protein travels multiple energy minima. The S(solv) considers the changes in the solvent configuration upon solvating the protein molecule, which originates from the hydrophobic effect, and may be approximated by a solvent accessible surface area (SASA) term.

In the following, we do not consider S(trans) and S(rot), since the variation in the moments of inertias are small among different systems studied here. The variation in S(solv) is estimated to be ~1 kcal/mol from the SASA model and is thus ignored.

The changes in the conformational entropy S(conf) include contributions from both side-chain and backbone motions. In the model by Pickett and Sternberg (32), side-chain contribution is calculated by assuming that the more solvent-exposed side chains can access different rotameric states, whereas a buried side chain is limited to a single rotamer. In the calculation of Noskov et al. (33), the contributions from S(conf) and S(solv) offset each other to a large degree.

For this study, we estimate the contribution from S(vibr) to assess the changes in the rigidity of the protein upon ion bindings. This is done by calculating the 3N-6 quasiharmonic modes of the system and evaluating the quasiharmonic entropy S(vibr) using the following formula:

$$\mathrm{TS(vibr)} = \sum_{i=1}^{3N-6}\left[\frac{hv(i)}{e^{\mathrm{hv(i)}}/kT - 1} - kT\ln(1 - e^{\mathrm{hv(i)}}/kT)\right], \quad (2)$$

where $v(i)$ is the ith quasiharmonic mode, k is the Boltzmann constant, and h is the Planck constant.

The VIBRAN module in CHARMm was used to perform the quasiharmonic analysis. In this method, atom position fluctuation tensors are generated. The resulting fluctuation matrix is mass weighted and diagonalized to obtain the quasiharmonic modes of the system. The protein translation and rotation were removed from the dynamics trajectory, and only the internal motions were included in the calculation of the quasiharmonic modes.

Calculated vibrational entropies for different systems are given in Table 3 and Fig. 4. The convergence of the S(vibr) with increasing the trajectory length is shown in Fig. 4 *a*. The calculations did not fully converge within the 4-ns trajectories, but the curves begin to level off and reach a plateau near the end of the trajectory. Starting from 3 ns, the rank order of the entropies of the six systems remain essentially unchanged if the small relative variations of ≤5 kcal/mol between 0Cu and H-13 are ignored (Table 3). We therefore based our discussion on the data set obtained at 4 ns (Table 4).

As can be seen from Tables 3 and 4, H-31 and 3Cu have a similar and the largest TS(vibr), ~68 kcal/mol above the native system 0Cu. The TS(vibr) in the 2Cu system are ~32 kcal/mol larger than the values for the native state. These vibrational entropy differences are of the same magnitude as the $T\Delta S$(vibr) between the native and denatured proteins of similar size (27,28). In the H-51 system, the TS(vibr) is ~15 kcal/mol higher than the two native-like systems 0Cu and H-13.

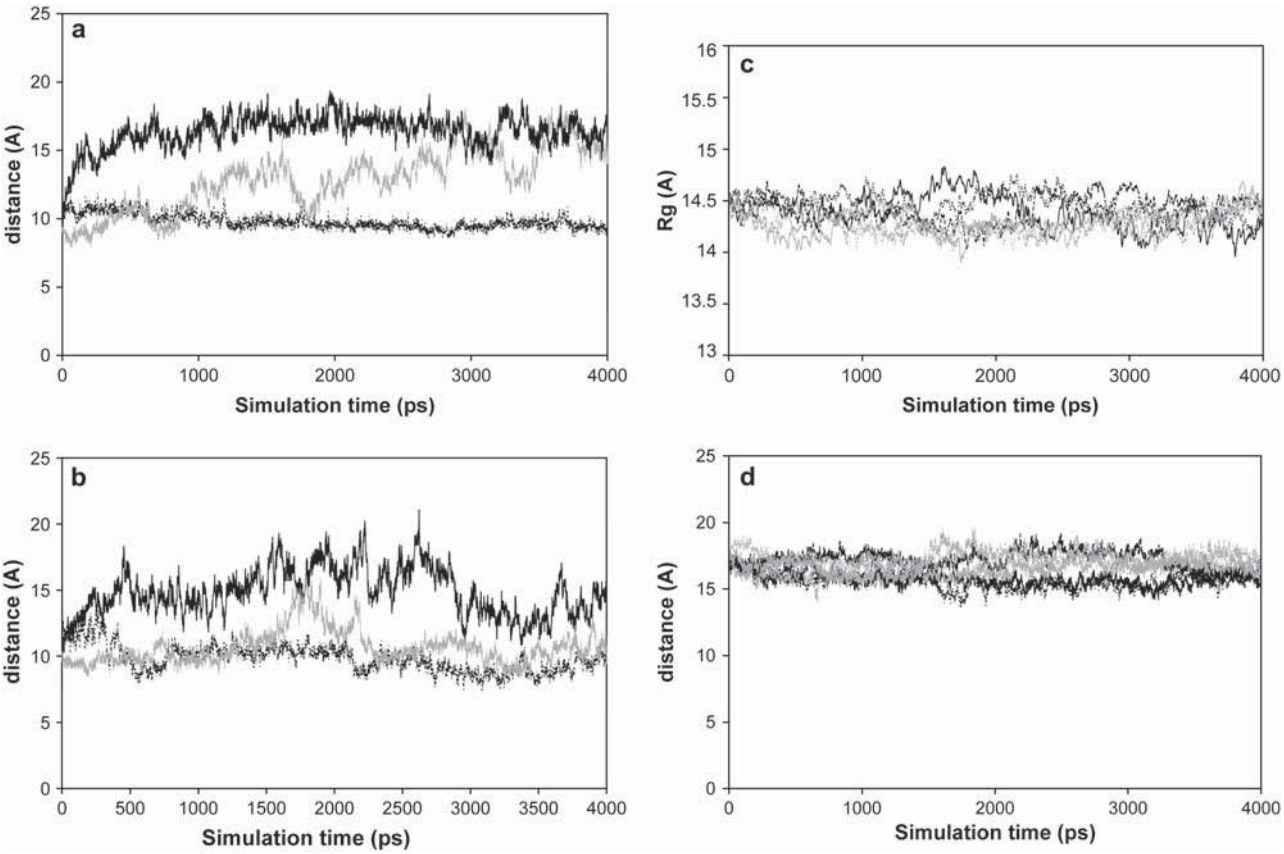

FIGURE 7 (*a*) Distance between the center of mass of the D-E loop and that of the B-C loop for 0Cu (*black*, *dashed*), 2Cu (*gray*, *solid*), and 3Cu (*black*, *solid*). (*b*) Same as in (*a*) for H-13 (*black*, *dashed*), H-51 (*gray*, *solid*), and H-31 (*black solid*). (*c*) Radius of gyration of the protein molecule. The color codes are the same as those in Fig. 4 *b*. (*d*) Distance between the protein center of mass and the center of mass of the D-E loop. The color codes are the same as those in Fig. 4 *b*.

We noted that the accuracy of the entropy calculation is limited by at least two factors. The first is the lack of complete convergence, as a result of the limited sampling of phase space. This may explain why the 2Cu system has a lower S(vibr) than both the H-31 and 3Cu systems. The second factor comes from the quasiharmonic approximation, which assumes a multivariate Gaussian distribution for protein dynamics (see Chang et al. (37) for a recent study). However, within the error of the these calculations, the rank order of the entropy reproduces the results from RMSD analysis (Figs. 2 and 3 and later Fig. 5, *d* and *e*), and the magnitude of the entropy change are in the same range as the entropy of protein denaturation from earlier work (27,28). Taken together they provide evidence for conformational transitions toward more disordered states with less rigidity in the 2Cu, H-31, 3Cu, and to a lesser extent H-51 systems (see Table 4).

TABLE 5 Ratio between the extent of the first and second principal axes

	0Cu	2Cu	3Cu	H-13	H-31	H-51
x_{ext}/y_{ext}	1.27	1.21	1.18	1.33	1.09	1.41

NMR order parameter and Cα RMSF

NMR order parameter S^2 is frequently monitored in the study of protein and polypeptide backbone dynamics by heteronuclear ^{15}N-^{1}H relaxation (30,31,34), in which the relaxation due to internal motion is analyzed in the framework of the Lipari-Szabo formula (29). Recent theoretical and experimental work attempts to relate the NMR-derived order parameter with thermodynamic properties such as entropy (27,36). In a case study of the native and denatured staphylococcal nuclease, Wrabl et al. (27) have shown that changes in the NMR order parameter are correlated with the conformational entropy of the protein and that ~25% of the entropy change may be attributed to the changes in local entropy reflected by S^2.

In this study, we analyze the order parameter S^2 to obtain residue-specific dynamics information and evaluate the possible impact from bound Cu^{2+} on the residues near the ion-binding sites. The N-H vector order parameter S^2 was obtained from the long time limit of the autocorrelation function $C(t)$, $S^2 = \lim_{t->\infty} C(t)$, where

$$C(t) = A\langle P_2[\mu(\tau)\mu(\tau + t)]/r^3(\tau)r^3(\tau + t)\rangle \qquad (3)$$

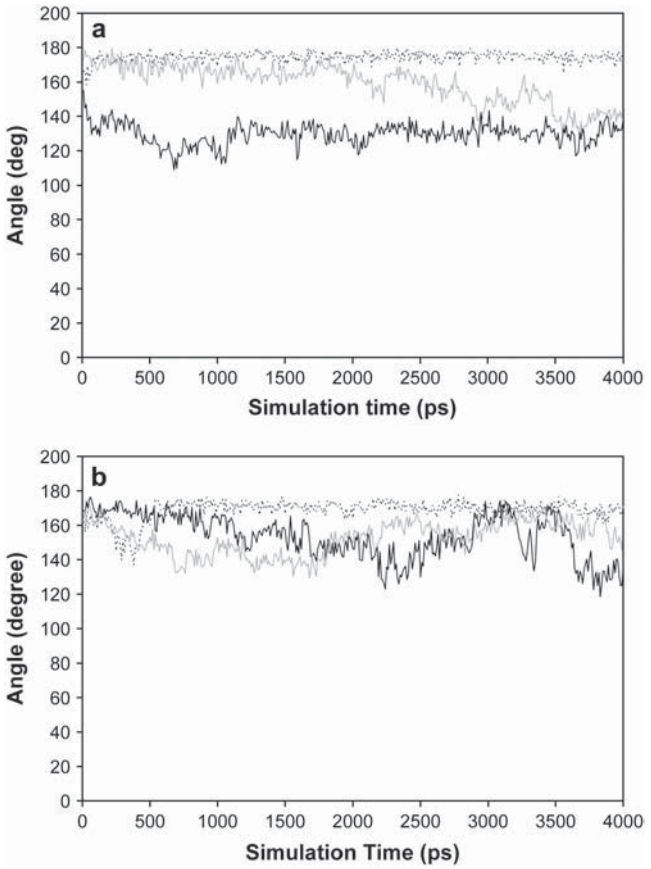

FIGURE 8 Time evolution of the angle between the vector connecting the Cα atoms of the residues 50/54 and that connecting the Cα atoms of the residues 65/68. (*a*) 0Cu (*black*, *dashed*), 2Cu (*gray*, *solid*), and 3Cu (*black*, *solid*). (*b*) H-13 (*black*, *dashed*), H-51 (*gray*, *solid*), and H-31 (*black solid*).

A is a constant that makes $C(0) = 1$. P_2 is the second Legendre polynomial $P_2[x] = 1/2(3x^2 - 1)$; $\mu(\tau)$is the unit vector for the orientation of the N-H bond relative to a fixed reference frame, which is the first coordinate frame of the trajectory. The global rotational motion was removed by superimposing each trajectory frame onto this reference frame; $r(\tau)$ is the N-H bond length, whose effect is ignored because its variation is negligible.

The autocorrelation function $C(t)$ for each residue—except proline residues, which lack the N-H bond—was calculated for 1024 ps, i.e., approximately one-fourth of the total trajectory length of 4 ns. From visual inspection of $C(t)$, it can be stated that some residues did not fully converge within 1 ns. One such example for residue 62 is given in Fig. 5 *a*. In the following calculations, the average value during the last 24 ps of the trajectory was used, which should be viewed as an upper limit for the real S^2.

The simulated residue-specific S^2 results are given in Fig. 5, *b* and *c*. For comparison, the corresponding residue-specific RMS fluctuations (RMSF) for Cα atom are shown in Fig. 5, *d* and *e*. Not surprisingly, the S^2 values are inversely correlated with the RMSF along the protein backbone, where the low values of S^2 occur in the loops between β-strands. Among the simulated systems, the differences in S^2 and RMSF were large in the loops and in the edges of the β-strands. In particular, the B-C loop (residues 30–33) and the D-E loop (residues 53–64) displayed heightened motions (low S^2 and high RMSF) in H-31, 2Cu, and 3Cu systems, compared with those in 0Cu and H-13 systems. In this region, residues 30–33 and residues 57–64 were within 5 Å from the His-31-binding site, whereas residues 53–56 were located close to the His-51-binding site.

In the H-51 system, residues 52–62 showed lower S^2, which means increased backbone dynamics and is in agreement with the results of the NMR study of Villanueva et al. (14). However, the corresponding RMSFs for these residues were only slightly higher than those in the H-13 system. This discrepancy indicates that the S^2 order parameter for the N-H vector does not fully reflect the RMSF at the Cα position. The overall results for the order parameter S^2 and Cα RMSF are consistent with the ranking order of the vibrational entropy for the simulated systems (Table 4).

Molecule size and shape

Snapshots of the trajectories taken at 3.5 ns and at 4 ns illustrate the striking differences in the representative conformations sampled for different systems (Fig. 6, *a* and *b*). It can be seen that in the lower half of the structures of the 2Cu, 3Cu, and H-31 systems, the protein adopted a substantially less compact conformation compared with the structures in both 0Cu and H-13 snapshots, in which the native fold was maintained. Compared with the native structure represented by the 0Cu snapshots, the E strand in the 3Cu snapshots was shorter by five residues at 3.5 ns and by two residues at 4 ns. The D strand was unstable in the 3Cu snapshots and in the 4-ns snapshot for the H-31 simulation. Much of the increase in the disorder in these structures involved the segment containing residues 49–63, which comprise the β-strands D2, the D-E loop, and the lower end of the E strand in the native structure. In 2Cu, 3Cu, and H-31 simulations, the D-E loop moved away from the B-C loop by ~6 Å, compared with native structure (see Fig. 7, *a* and *b*). This movement of the D-E loop was also observed in the H-51 simulation for a brief period from 1.6 ns to 2.3 ns. The protein in the H-31, 2Cu, and 3Cu snapshots became more spherical. To confirm this observation, the ratio between the extents of the molecule along the first two principal axes, x_{ext}/y_{ext}, are calculated for different systems (Table 5). In the calculation of x_{ext} and y_{ext}, the protein was first centered about the origin and then rotated to align with the principal axes for the moments of inertia, i.e., its principal axis coincides with the x axis and the second largest axis coincides with the y axis. In Table 5, the averaged values of x_{ext}/y_{ext} for each frame of the last 2 ns of the trajectory are presented. It is apparent that the molecule in the H-31, 3Cu, and to a lesser extent 2Cu simulations is less elongate in the x-y plane.

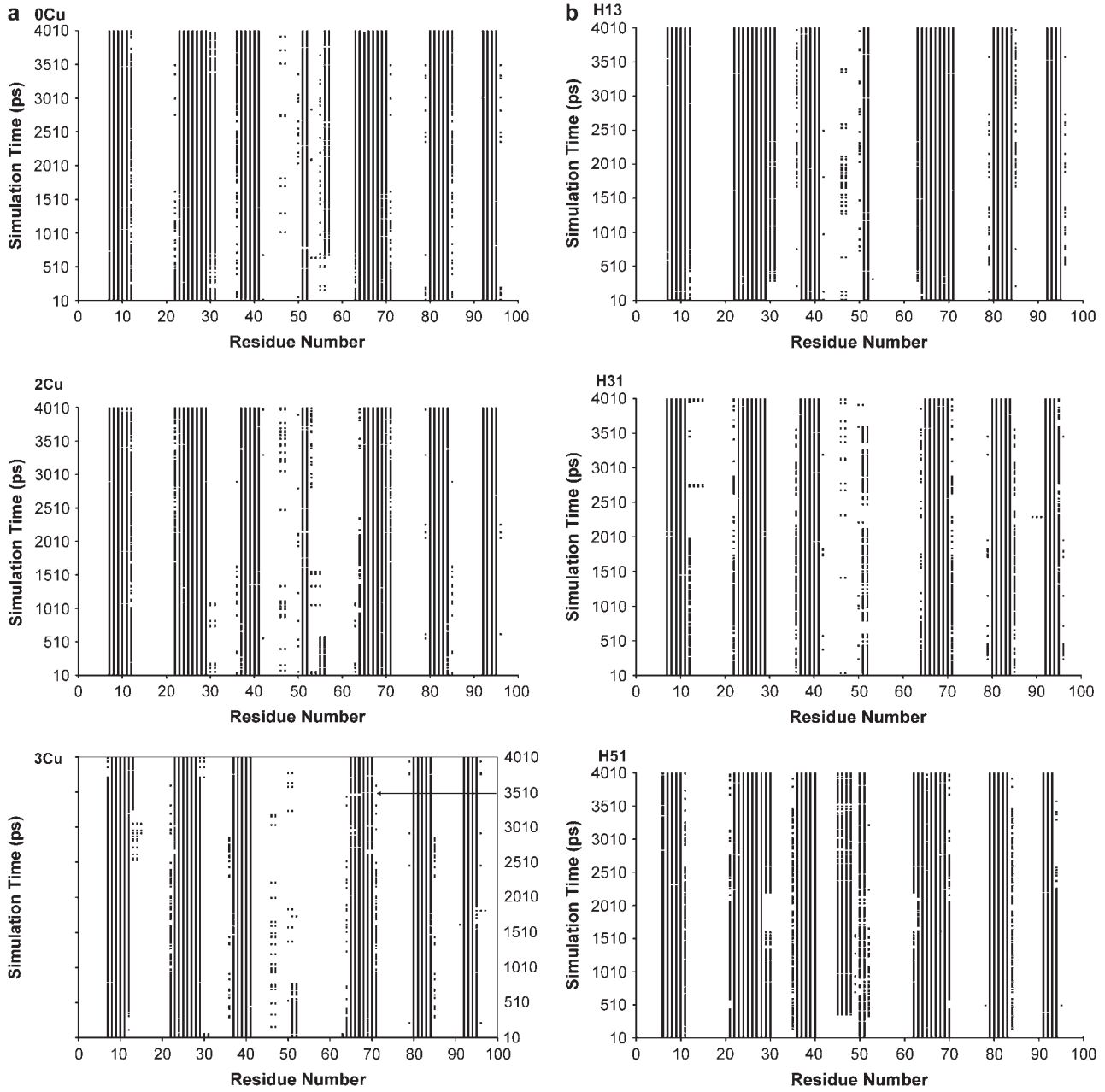

FIGURE 9 Time evolution of the secondary structure along MD trajectories. The black points represent residues in β-strands. The E strand in the 3Cu trajectory was briefly shortened by >60% between 3.46 and 3.5 ns, as indicated by the arrow in the figure.

However, the change in the shape of the molecule was not reflected in the radius of gyration, which remained unchanged (Fig. 7 *c*). To understand this somewhat surprising result, we calculated the distance between the center of mass of the D-E loop and the molecule center (Fig. 7 *d*), which also remained unchanged as the contents of bound ions were varied. Comparing the results of Fig. 7 *d* and those of Fig. 7, *a* and *b*, and examining the D-E loop conformation, we find that the movement of the D-E loop involved local fluctuations in the loop conformation and segment rotations about the molecule center of mass. This swing motion and local fluctuation of the D-E loop did not lead to significant changes in the radius of gyration.

In the 2Cu, 3Cu, H-31, and H-51 simulations, the residues 50–54 underwent a rigid body rotation (see Fig. 8). These residues were adjacent to the D-E loop and included the two-residue D2 strand. During the course of the simulations this segment rotated ~40° away from the initial antiparallel orientation relative to the neighboring E strand, as demonstrated by the change in the angle between the vector connecting the Cα atoms of residues 50/54 and the vector connecting the Cα atoms of residues 65/68 (Fig. 8). In the

2Cu simulation, this rotation starts at around 1.95 ns, which coincided with the rise in RMSD in this system discussed earlier (Figs. 2 and 3). This feature was absent in the 0Cu and H-13 simulations.

Stability of secondary structure

To characterize the effect of the Cu^{2+} on the stability of the β-sheets, we present the temporal history of the secondary structure for the simulated systems (Fig. 9). As can be seen, the main features of the β-sheets structure were largely retained for all the systems, i.e., the β-strands ABC and EFG were preserved throughout the 4-ns simulation. In all the simulated systems except H-51, the two-residue β-strand D1 had a very low occupancy. Fig. 9 reveals some noticeable differences in the length and the stability of β-strands among the simulated systems. Although the D2 strand (in H-51 it consists of residues 49–50) persisted in the 0Cu, H-13, and 2Cu simulations, this strand became unstable from 3.6 ns in the H-31 trajectory and was disrupted in the 3Cu simulation from 0.78 ns, which roughly coincides with the major conformational change in the 3Cu system revealed by the RMSD results in Figs. 2 and 3. A two-residue β-strand comprising residues 55–56 was observed in the 0Cu simulation. This strand was also present in the NMR solution structure family with a low occupancy (three out of 20; see Verdone et al. (12)). In the H-51 simulation, residues 44–47 form a β-strand, which corresponds to the D1 strand observed in the NMR structures of β2m (Table 1).

Shortening in the length of the β-strands was observed in H-31, 2Cu, and 3Cu systems (Fig. 9, Table 6). For example, in the 3Cu system the lengths of the strand B and E were each shortened by two residues and the strand C and F were each shortened by one residue. As seen from the snapshot in Fig. 6 *a* and from Fig. 9, in the 3Cu system the E strand was shortened by ~60% between 3.46 ns and 3.5 ns. In the 2Cu system, these four strands were each shortened by one residue. The regions where the β-strands B, C, and E were shortened are near the Cu^{2+}-binding site at His-31. The D2 strand is close to the His-51-binding site. Whereas residues near His-31 and His-51 underwent substantial changes in the secondary structure, the effects on residues in more distant regions are small. One exception is the G strand in the H-51 simulation, shortened by one residue starting from 2.3 ns. It is unclear whether this is an effect of the bound ion at His-51, since the feature was absent in the 3Cu system, which also has a Cu^{2+} ion at His-51.

Changes in the β-sheet structure are associated with the changes in the main chain hydrogen bond pattern for those affected residues. Examination of the hydrogen bond patterns involving β-strands B-D-E reveals significant differences among the simulated systems (Fig. 10). The backbone hydrogen bonds formed at the lower edges of the β-strands B and E, which are near the His-31 site, were stable in the 0Cu, H-13, and H-51 systems but were disrupted in the H-31, 2Cu, and 3Cu systems, which caused partial separation between the two strands at the lower end of the β-sheet. The hydrogen bonds in the upper half of the β-sheet were not noticeably affected. This qualitative observation is confirmed by the result of time occupancy of the main chain hydrogen bonds in β-sheet B-D-E (Table 7). For example, in the 3Cu system between the B and E strands, the main chain hydrogen bonds Phe-30O-Phe-62H, Gly-29H-Phe-62O, Val-27H-Leu-64O, Val-27O-Leu-64H, and Cys-25O-Tyr-66H had lowered occupancies of 0%, 0%, 76%, 65%, and 42% respectively. As discussed above, these residues that are located near the Cu^{2+}-binding site at His-31 also showed disruptions in β-strand conformations (Table 6). Some perturbations to the hydrogen bonds between the D and E strands, such as Glu-50H-Tyr-67O and Ser-52H-Leu-65O, occurred in the 3Cu, H-51, and H-31 simulations.

In Fig. 11, we present the nonbonded interaction energy between the β-strands B and E, which provides an estimate for the disruptions to the native compactness near the copper-binding sites His-31 and His-51. On average, the interactions between these two strands in the H-31, 2Cu, and 3Cu systems were weaker than those in the 0Cu and H-13 systems by 10–20 kcal/mol. In the H-51 simulations, the nonbonded interactions were also weakened by 10–15 kcal/mol between 1.6 ns and 2.2 ns, which coincided with the movement of the D-E loop seen in Fig. 7 *b*. A significantly smaller difference of 1–5 kcal/mol between the 0Cu and 1Cu systems was observed, illustrating the close resemblance in the conformations adopted by the two systems in this part of

TABLE 6 Residue compositions of β-strands in the simulated systems

β-strand*	0Cu	H-13	2Cu	3Cu	H-31	H-51†
A	6–11	6–11	6–11	6–11	6–10	5–10
B	22–30	21–30	**21–28**	**22–28**	**22–28**	21–29
C	35–40	35–40	**36–40**	**36–40**	35–40	34–39
D2	50–51	50–51	50–51	**none**	50–51	49–50
E	62–69	62–70	**64–70**	**64–69**	**64–69**	61–68
F	79–84	79–83	79–83	79–83	79–84	78–83
G	91–94	91–94	91–94	91–94	91–94	**90–92**

*A residue is counted only if it has a β-strand occupancy of 60% or higher during the last 3 ns of the simulation. β-strands that displayed shortening in length are shown in bold.

†The D1 strand formed by residues 44–47 in the H-51 system was not listed in the table.

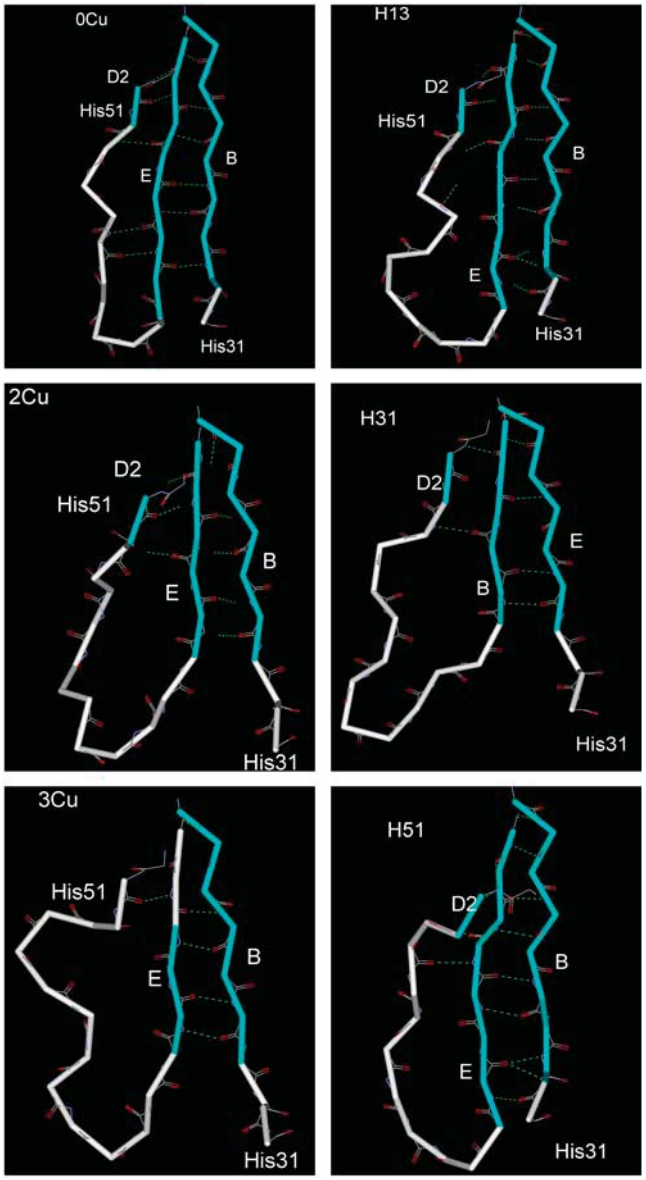

FIGURE 10 The hydrogen bond pattern and the main chain conformation of the segment containing β-strand B (residues 22–31), D2, and E (residues 49–68). The structures are from snapshots taken at 3.5 ns.

the structure. The disruption of the nonbonded interaction is closely related to the changes in the hydrogen bond pattern (Table 7) and it contributed to the loosening of the molecule, which is reflected by the vibrational entropy increase.

Solvent exposure near ion-binding sites

The extent of the copper-induced structural rearrangement can also be seen from the changes in the solvent exposure of the groups located near the copper-binding sites at His-31 and His-51 (Figs. 12 and 13). The two segments that became more exposed to the solvent upon Cu^{2+} binding are the D-E loop (residues 52–63) and the B-C loop (residues 30–33)

TABLE 7 Time occupancy of backbone hydrogen bonds (%)

Strands*	Hydrogen bonds	0Cu	2Cu	3Cu	H-13	H-31	H-51
B-E	Phe-30O-Phe-62H	47	**0**	**0**	70	**0**	74
	Phe-30H-Phe-62O	30	**0**	**0**	67	**0**	45
	Gly-29H-Phe-62O	80	**20**	**0**	**30**	**16**	**54**
	Val-27H-Leu-64O	93	88	**76**	94	88	84
	Val-27O-Leu-64H	90	**76**	**65**	**72**	92	**75**
	Cys-25O-Tyr-66H	93	86	**42**	94	**47**	79
	Cys-25H-Tyr-66O	100	99	96	99	93	97
	Leu-23H-Thr-68O	98	94	85	96	98	96
	Leu-23O-Thr-68H	70	63	61	67	68	63
D-E	Glu-50O-Tyr-67H	90	90	94	92	84	**75**
	Glu-50H-Tyr-67O	90	81	**74**	82	84	**20**
	Ser-52H-Leu-65O	54	52	**0**	58	**18**	78
D-E	Ser-55O-Tyr-63H	68	**0**	**0**	**0**	**0**	**0**

*Hydrogen bonds that experienced significant disruptions (>10% reduction) relative to 0Cu trajectory are shown in bold.

(see Table 8). Some of these residues, such as Ser-55 and Tyr-63, form main chain hydrogen bonds, whereas others maintain hydrophobic contacts (e.g., Phe-30, Phe-62) in the absence of copper. These native contacts at the lower edge of the protein protect the hydrophobic core from the solvent in the folded state.

DISCUSSION

Driving force for Cu^{2+}-induced destabilization

In these MD simulations, transitions to more disordered conformations were observed in the nanosecond timescale in the presence of copper ions. The partially unfolded conformation is less elongate, and the structure is characterized by disruptions of certain secondary structures and hydrogen bonds and an increase in the solvent exposure for groups located near the ion-binding sites. The weakening in the native interactions leads to an increase in atomic fluctuations and configurational entropy. From the molecular mechanics point of view, the binding of a Cu^{2+} ion effectively adds a $+2e$ charge to the histidine side chain, as the Cu^{2+} ion has a small van der Waals radius of 1.38 Å. The effect of the copper ion can be understood by considering the change in the electrostatic properties. The addition of $+2e$ charges increases both the range and magnitude of the electrostatic interactions and makes the binding site more polar, which induces water molecules to compete with neighboring protein groups for optimal contacts with the bound ion. During this process, neighboring residues that form native contacts are displaced by solvent molecules, which results in an increased exposure for those groups that are found buried in the native state. The acceleration in the transition toward the partially unfolded state in the presence of copper in the nanosecond timescale suggests that the ion binding has lowered the barrier of the conformational transition as a result of changes in the hydrophobic/hydrophilic environment in the vicinity of the ion-binding site.

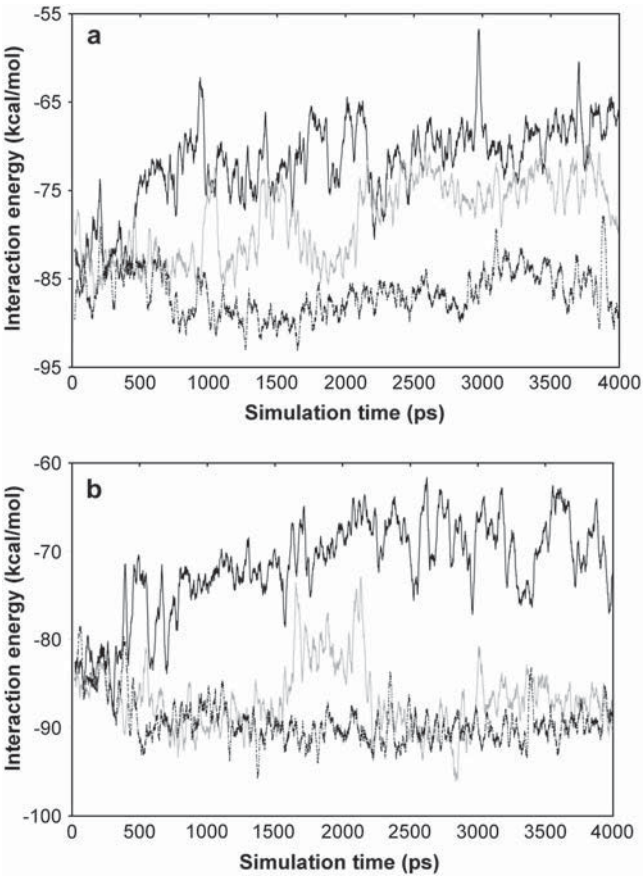

FIGURE 11 Time series of the nonbonded interaction energy between β-strands B and E. The 10-ps block averaged results are shown. (*a*) 0Cu (*black*, *dashed*), 2Cu (*gray*, *solid*), and 3Cu (*black*, *solid*). (*b*) H-13 (*black*, *dashed*), H-51 (*gray*, *solid*), and H-31 (*black solid*).

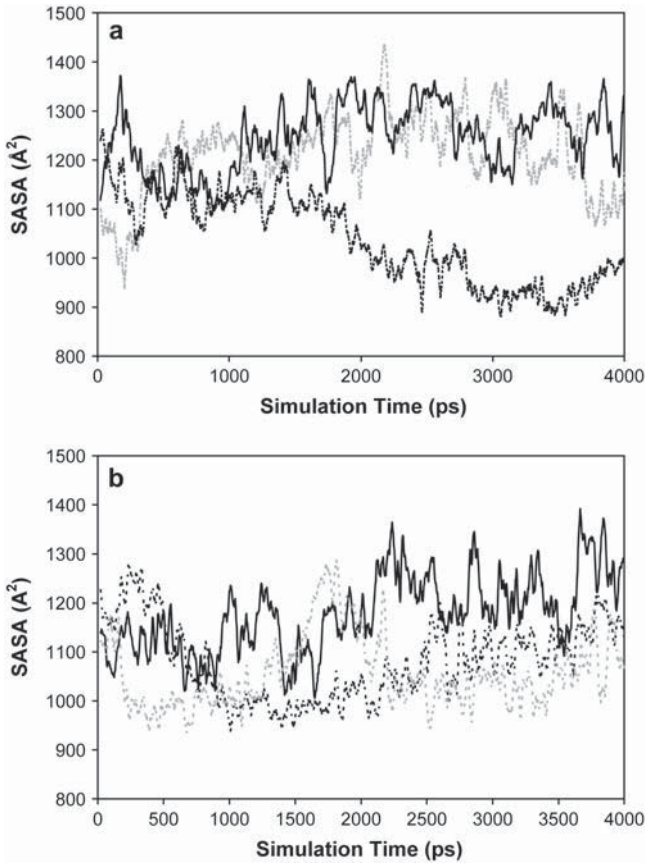

FIGURE 12 SASAs as functions of the simulation time for residues connecting strands D and E (residues 52–63). The 10-ps block averaged results are shown. (*a*) 0Cu (*black*, *dashed*), 2Cu (*gray*, *dashed*), and 3Cu (*black*, *solid*). (*b*) H-13 (*black*, *dashed*), H-51 (*gray*, *dashed*), and H-31 (*black solid*).

As mentioned in the introduction, one explanation for the copper-induced destabilization is based on the increased affinity for copper in the denatured states compared with the native state (13), which may result from increased solvent exposure of potential copper-binding histidines in the denatured state. In the study by Eakin et al., they found that in the native state only His-31 binds copper, whereas in the nonnative states His-13, His-51, and His-84 bind copper. In the native state, His-84 is completely buried and His-31 is 62% buried, whereas His-13 and His-51 are significantly exposed (~70%). Although the most buried, His-84, is likely to become accessible for the binding of copper in the denatured states, it is difficult to see how His-31 loses its ability to bind copper in the nonnative conformations where it becomes more exposed. That the more exposed His-13 and His-51 do not bind copper in the native state is also puzzling. In addition, this model may not explain the copper-induced stabilization of conformations that are only partially unfolded. These intermediate states are believed to be the precursor for the formation of amyloid fibrils. Some evidence suggests that the unfolding intermediate states retain much of the secondary structure and some native tertiary structures. Recently, Eakin et al. (35) have monitored the formation of oligomeric intermediates of β2m along the fibrillogenesis pathway induced by Cu^{2+}. They found that the Cu^{2+}-induced amyloid formation does not require global destabilization of β2m, and the native-like oligomeric intermediates form fibrils by domain swapping. Their results suggest that Cu^{2+} mediates the formation of an activated monomeric state. In this context, the results of these MD simulations demonstrate a correlation between the specific binding of copper in the native state and the acceleration in the conversion to the partially unfolded conformations. It is possible that this finding is relevant to the increases in the population of the intermediate states in the presence of copper.

Comparisons with experiments

NMR studies revealed evidences for the changes in the conformation and dynamics due to Cu^{2+} binding. Attenuation in the peak intensities of ^1H-^{15}N HSQC spectra due to paramagnetic perturbation from Cu^{2+} is reported for residues located near His-31 in several investigations (12–14).

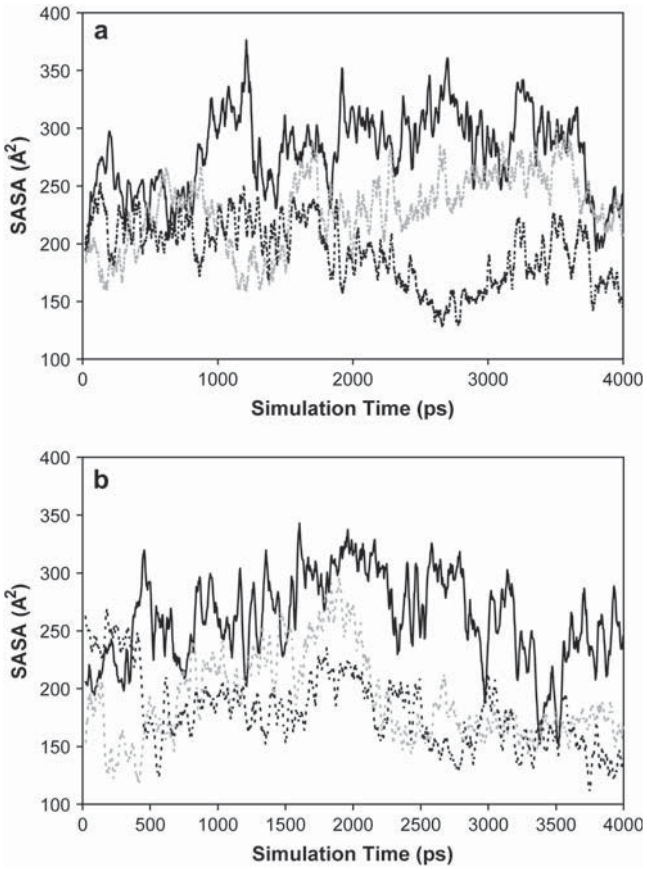

FIGURE 13 SASAs as functions of the simulation time for residues connecting strands B and C (residues 30–33). The 10-ps block averaged results are shown. (*a*) 0Cu (*black*, *dashed*), 2Cu (*gray*, *dashed*), and 3Cu (*black*, *solid*). (*b*) H-13 (*black*, *dashed*), H-51 (*gray*, *dashed*), and H-31 (*black solid*).

Separately, Villanueva et al. showed that the spectra for residues close to His-51 are also perturbed by the copper ion (14). In this study, we have seen an association between major conformational changes and the Cu^{2+} binding at His-31 and His-51. In addition, the results presented here suggest that although the Cu^{2+} binding at His-51 contributed to the increased conformational dynamics, the His-31 is a more effective ion-binding site in destabilizing the native protein.

The reduction in the peak intensities for residues close to His-13 are also reported, indicating that this histidine is also involved in the specific binding of copper (12,14). His-13 resides in the loop connecting strand A and B. Both the solution NMR study at native conditions (12) and our control simulation of apo-β2m at 300 K showed that this loop is dynamic in solution, associated with large RMS deviation (results not shown). In this study, the dynamic nature of this region does not appear to undergo significant change in any of the simulations in the presence of Cu^{2+}. Given the striking similarity between the behaviors of 0Cu and H-13 simulations, we conclude that although His-13 may bind copper in the native state, this specific binding does not have a major influence on the conformational properties of β2m.

TABLE 8 Solvent accessible surface area (in units of Å²)

	0Cu	2Cu	3Cu	H-13	H-31	H-51
Residue 52–63	1007	1229	1268	1063	1200	1071
Residue 30–33	186	235	289	173	266	194

Information on the changes of the backbone dynamics due to Cu^{2+} binding have been deduced from steady-state ^{1}H-^{15}N NOE values (14,19). After correcting for the paramagnetic contributions from Cu^{2+}, Asp-49 and Ser-55 on the strand D are found to display an increase in backbone dynamics in the pico- to nanosecond timescale, which was attributed to the effect of Cu^{2+} binding at His-51 by Villanueva and co-workers (14). In this study, increases in the chain flexibility at the segment level are inferred from analysis of the multiple nanoseconds MD simulations. Overall, we see a qualitative agreement between the results of the present MD simulation and NMR experiments regarding the increased conformational dynamics involving the strand D and its neighboring groups upon ion binding. However, in contrast to the conclusions of Villanueva et al. (14), our simulation data suggested that the changes in the chain flexibility are primarily derived from the Cu^{2+} binding at His-31, instead of from the His-51-binding site. As an example, the D2 strand was disrupted in the 3Cu simulation and near the end of the H-31 simulation, yet it remained stable in the H-51 simulation (Fig. 9) although a rigid body rotation involving residues 50–54 was observed in H-51 system and in 2Cu, H-31, and 3Cu systems (Fig. 8). We note that contributions to conformational transitions from different copper-binding sites are not readily separable in NMR experiments, whereas for such problems important insights can be obtained from molecular simulation.

We thank Dr. John Clark for his help with the DS Modeling program, Dr. Deqiang Zhang for his help with computer graphics, Dr. Taisung Lee for helpful discussions regarding the manuscript, and Mr. Christopher Strauss for his effort in providing technical support to the computing facilities.

REFERENCES

1. Yamashita, M. M., L. Wesson, G. Eisenman, and D. Eisenberg. 1990. Where metal ions bind in proteins. *Proc. Natl. Acad. Sci. USA.* 87: 5648–5652.
2. Werner, J. M., V. Knott, P. A. Handford, I. D. Campbell, and A. K. Downing. 2000. Backbone dynamics of a cbEGF domain pair in the presence of calcium. *J. Mol. Biol.* 296:1065–1078.
3. Akke, M., N. J. Skelton, J. Kordel, A. G. Palmer 3rd, and W. J. Chazin. 1993. Effects of ion binding on the backbone dynamics of calbindin D9k determined by 15N NMR relaxation. *Biochemistry.* 32:9832–9844.
4. Lins, R. D., J. M. Briggs, T. P. Straatsma, H. A. Carlson, J. Greenwald, S. Choe, and J. A. McCammon. 1999. Molecular dynamics studies on the HIV-1 integrase catalytic domain. *Biophys. J.* 76:2999–3011.
5. Gejyo, F., T. Yamada, S. Odani, Y. Nakagawa, M. Arakawa, T. Kunimoto, H. Katoka, M. Suzuki, Y. Hirasawa, T. Shirahama, A. S. Cohen, and K. Schmid. 1985. A new form of amyloid protein

associated with hemodialysis was identified as β2-microglobulin. *Biochem. Biophys. Res. Commun.* 129:701–706.

6. Bjorkman, P. J., M. A. Saper, B. Samraoui, W. S. Bennett, J. L. Strominger, and D. C. Wiley. 1987. Structure of the human class I histocompatibility antigen, HLA-A2. *Nature.* 329:506–512.
7. Floege, J., and G. Ehlerding. 1996. Beta-2-microglobulin-associated amyloidosis. *Nephron.* 72:9–26.
8. Okon, M., P. Bray, and D. Vucelic. 1992. 1H NMR assignments and secondary structure of human β2-microglobulin in solution. *Biochemistry.* 31:8906–8915.
9. Kad, N. M., N. H. Thomson, D. P. Smith, D. A. Smith, and S. E. Radford. 2001. Beta(2)-microglobulin and its deamidated variant, N17D form amyloid fibrils with a range of morphologies in vitro. *J. Mol. Biol.* 313:559–571.
10. Esposito, G., R. Michelutti, G. Verdone, P. Viglino, H. Hernandez, C. V. Robinson, A. Amoresano, F. Dal Piaz, M. Monti, P. Pucci, P. Mangione, M. Stoppini, G. Merlini, G. Ferri, and V. Bellotti. 2000. Removal of the N-terminal hexapeptide from human beta2-microglobulin facilitates protein aggregation and fibril formation. *Protein Sci.* 9:831–845.
11. Morgan, C. J., M. Gelfand, C. Atreya, and A. D. Miranker. 2001. Kidney dialysis-associated amyloidosis: a molecular role for copper in fiber formation. *J. Mol. Biol.* 309:339–345.
12. Verdone, G., A. Corazza, P. Viglino, F. Pettirossi, S. Giorgetti, P. Mangione, A. Andreola, M. Stoppini, V. Bellotti, and G. Esposito. 2002. The solution structure of human beta2-microglobulin reveals the prodromes of its amyloid transition. *Protein Sci.* 11:487–499.
13. Eakin, C. M., J. D. Knight, C. J. Morgan, M. A. Gelfand, and A. D. Miranker. 2002. Formation of a copper specific binding site in non-native states of beta-2-microglobulin. *Biochemistry.* 41:10646–10656.
14. Villanueva, J., M. Hoshino, H. Katou, J. Kardos, K. Hasegawa, H. Naiki, and Y. Goto. 2004. Increase in the conformational flexibility of beta 2-microglobulin upon copper binding: a possible role for copper in dialysis-related amyloidosis. *Protein Sci.* 13:797–809.
15. Atwood, C. S., R. D. Moir, X. Huang, R. C. Scarpa, N. M. Bacarra, D. M. Romano, M. A. Hartshorn, R. E. Tanzi, and A. I. Bush. 1998. Dramatic aggregation of Alzheimer abeta by Cu(II) is induced by conditions representing physiological acidosis. *J. Biol. Chem.* 273: 12817–12826.
16. Huang, X., C. S. Atwood, R. D. Moir, M. A. Hartshorn, J. P. Vonsattel, R. E. Tanzi, and A. I. Bush. 1997. Zinc-induced Alzheimer's Abeta1-40 aggregation is mediated by conformational factors. *J. Biol. Chem.* 272:26464–26470.
17. Kramer, M. L., H. D. Kratzin, B. Schmidt, A. Romer, O. Windl, S. Liemann, S. Hornemann, and H. Kretzschmar. 2001. Prion protein binds copper within the physiological concentration range. *J. Biol. Chem.* 276:16711–16719.
18. Davis, D. P., G. Gallo, S. M. Vogen, J. L. Dul, K. L. Sciarretta, A. Kumar, R. Raffen, F. J. Stevens, and Y. Argon. 2001. Both the environment and somatic mutations govern the aggregation pathway of pathogenic immunoglobulin light chain. *J. Mol. Biol.* 313:1021–1034.
19. Viles, J. H., D. Donne, G. Kroon, S. B. Prusiner, F. E. Cohen, H. J. Dyson, and P. E. Wright. 2001. Local structural plasticity of the prion protein. Analysis of NMR relaxation dynamics. *Biochemistry.* 40: 2743–2753.
20. Brooks, B. R., R. E. Bruccoleri, B. D. Olafson, D. J. States, S. Swaminathan, and M. Karplus. 1983. CHARMM: a program for macromolecular energy, minimization, and dynamics calculations. *J. Comput. Chem.* 4:187–217.
21. MacKerell, A. D. Jr., D. Bashford, M. Bellot, R. L. Dunbrack Jr., J. D. Evanseck, M. J. Field, S. Fischer, J. Gao, H. Guo, S. Ha, D. Joseph-McCarthy, L. Kuchnir, et al. 1998. All-atom empirical potential for molecular modeling and dynamics studies of proteins. *J. Phys. Chem. B.* 102:3586–3616.
22. Momany, F. A., and R. Rone. 1992. Validation of the general purpose QUANTA 3.2/CHARMm forcefield. *J. Comput. Chem.* 13: 888–900.
23. Jorgensen, W. L., J. Chandrashekhar, J. D. Madura, R. W. Impey, and M. L. Klein. 1983. Comparison of simple potential functions for simulating liquid water. *J. Chem. Phys.* 79:926–935.
24. Essmann, U., L. Perera, M. L. Berkowitz, T. Darden, H. Lee, and L. Pedersen. 1995. A smooth particle mesh Ewald method. *J. Chem. Phys.* 103:8577–8593.
25. Hoover, W. G. 1985. Canonical dynamics: equilibrium phase-space distributions. *Phys. Rev. A.* 31:1695–1697.
26. Kabsch, W., and C. Sander. 1983. Dictionary of protein secondary structure: pattern recognition of hydrogen-bonded and geometrical features. *Biopolymers.* 22:2577–2637.
27. Wrabl, J., D. Shortle, and T. Woolf. 2000. Correlation between changes in nuclear magnetic resonance order parameters and conformational entropy: molecular dynamics simulations of native and denatured staphylococcal nuclease. *Proteins.* 38:123–133.
28. Karplus, M., T. Ichiye, and B. Pettitt. 1987. Configurational entropy of native proteins. *Biophys. J.* 52:1083–1085.
29. Lipari, G., and A. Szabo. 1982. Model-free approach to the interpretation of nuclear magnetic resonance relaxation in macromolecules. *J. Am. Chem. Soc.* 104:4546–4558.
30. Clore, G., P. Driscoll, P. Wingfield, and A. Gronenborn. 1990. Analysis of backbone dynamics of interleukin-1b using two-dimensional inverse detected heteronuclear 15N-1H NMR spectroscopy. *Biochemistry.* 29:7387–7401.
31. Dayie, K., G. Wagner, and J. Lefèvre. 1996. Theory and practice of nuclear spin relaxation in proteins. *Annu. Rev. Phys. Chem.* 47: 243–282.
32. Pickett, S., and M. Sternberg. 1993. Empirical scaling of side-chain configurational entropy in protein folding. *J. Mol. Biol.* 231:825–839.
33. Noskov, S., and C. Lim. 2001. Free energy decomposition of protein-protein interactions. *Biophys. J.* 81:737–750.
34. Buck, M., and M. Karplus. 1999. Internal and overall peptide group motions in proteins: molecular dynamics simulations for lysozyme compared with results from x-ray and NMR spectroscopy. *J. Am. Chem. Soc.* 121:9645–9658.
35. Eakin, C., F. Attenello, C. Morgan, and A. Miranker. 2004. Oligomeric assembly of native-like precursors precedes amyloid formation by b-2 microglobulin. *Biochemistry.* 43:7808–7815.
36. Yang, D., and L. Kay. 1996. Contributions to conformational entropy arising from bond vector fluctuations measured from NMR-derived order parameters: application to protein folding. *J. Mol. Biol.* 263: 369–382.
37. Chang, C., W. Chen, and M. Gilson. 2005. Evaluating the accuracy of the quasiharmonic approximation. *J. Chem. Theory Comput.* 1: 1017–1028.